Article:

Li, X, Jiang, S, Ye, Y et al. (2018) Influence of random pore defects on failure mode and mechanical properties of SiC ceramics under uniaxial compression using discrete element method. Ceramics International, 44 (18). pp. 22271-22282. ISSN: 0272-8842

https://doi.org/10.1016/j.ceramint.2018.08.349

Influence of random pore defects on failure mode and mechanical properties of SiC ceramics under uniaxial compression using discrete element method

Xu Li[a], Shengqiang Jiang [a,*], Ying Ye[a], Sisi Liu[a], Zhiqiang Xu[a], Yuanqiang Tan[b] and Dongmin Yang[c]

[a]*School of Mechanical Engineering, Xiangtan University, Hunan, 411105, China*
[b]*Institute of Manufacturing Engineering, Huaqiao University, Fujian, 361021, China*
[c]*School of Civil Engineering, University of Leeds, Leeds, LS29JT, UK*

* Corresponding author. Tel.: +86 731 58292225. Fax: +86 731 58292209. *E-mail address: jsqcx@xtu.edu.cn*

Abstract: To investigate the relationship between micro defects in ceramic materials and macro mechanical properties and behaviours, a computational model of SiC ceramics with randomly oriented elliptical pores was established using the discrete element method (DEM). The effects of pore defect content and its aspect ratio on the failure mode, stress-strain curve and mechanical properties of specimen were investigated under uniaxial compression. The effective Young's modulus which was obtained from DEM simulations was compared with the predictions of Mori-Tanaka scheme (MTS) and Self-Consistent scheme (SCS) at various pore defect densities. The results showed that the compressive strength and crack initiation stress decrease nonlinearly as the pore defect content increases. Furthermore, the smaller the aspect ratio of the elliptical pore defects was, the more obvious the weakening trend was. As the pore defect content increases, the failure mode of the specimen changed from brittle fracture to tensile-shear mixing and then to axial splitting. The stress-strain curves showed a certain "softening" period during the loading process. The effective Young's modulus obtained from the DEM simulations coincides with the approximations of MTS and SCS at low pore densities. However, when the pore defect density became larger, the DEM simulation results were slightly lower than the theoretical results of the Mori-Tanaka scheme, which only considers the weak interaction between defects.

Keywords: Pore defect; Uniaxial compression; Mechanical properties; Discrete element method

1 Introduction

During the preparation process of ceramic materials, various random defects are introduced inevitably into the finished products due to unfavorable factors from materials and processes, such as excessive impurity content, uneven particle size distribution, unsatisfactory powder compaction and disappeared sintering-aid. Among those defects, the micropore defect is a typical and common type, as shown in Fig. 1 [1]. As a kind of hard and brittle material, ceramics are extremely sensitive to defects. The micropore defects with random orientation and distribution would affect the mechanical properties of the material and result in the dispersion of strength such that an unpredictable fracture failure could happen easily under the external load [2]-3]. Therefore, it is important to reveal the relationship between macroscopic failure and damage evolution which both are caused by internal microdefects.

Damage mechanics of brittle materials have been well developed in theory, such as Self-Consistent scheme [4], generalized Self-Consistent scheme [5], Differential scheme [6] and Mori-Tanaka scheme [7-8]. Although those methods can approximately calculate the effective modulus of specimen considering the interaction between defects, there is no agreement to decide which method is better unless the statistics of mutual positions of defects are specified. In addition, based on the manufacturing method of material defects, the effect of pre-existing artificial defects on the mechanical properties of specimen has also received extensive attention. How to prepare the specimen with controllable and quantifiable defects is usually crucial in experiment. In general, surface defects of brittle materials can be obtained easily by indentation [9] and laser processing [1], while the preparation of internal defects is relatively difficult to obtain. For instance, though the method of artificially pre-embedded carbon fiber can be used in internal defect preparation [10], the randomness problem of defect distribution yet cannot be solved accurately. Besides, X-ray computer tomography [11] and acoustic emission technology [12] can determine the location, size characteristics of defects and observe the cracking phenomenon. But it is difficult to record the micro-crack initiation, propagation and coalescence process between internal defects in real time. Meanwhile, it is easy to ignore the defect features because of the small size of defects in ceramic materials (micron level).

Numerical simulations provide a powerful complement to the experimental researches of micro cracking and damage around defects. The common numerical simulation techniques include the finite element method (FEM) [13], the numerical manifold method (NMM) [14], the discontinuous deformation analysis (DDA) [15], the boundary element method (BEM) [16] and realistic failure process analysis (RFPA) [17]. Although the fracture criterion and application of these methods are distinct, the research of crack initiation and propagation has been developed to some extent. Nevertheless, the details of crack propagation and coalescence between the defects cannot be presented clearly and the influence of micro-defects on the mechanical properties of materials on account of the randomness among the shape, position, size and orientation of the internal defects are not well clarified in brittle materials. Therefore, it is necessary to find a suitable and reliable numerical simulation method to solve the above problems. In our previous work, the authors have studied the effects of randomly oriented crack defects on failure modes and mechanical properties of SiC ceramics using DEM simulations [19]. However, in addition to the study of pre-crack defects, it is equally important to study the influence of pore defects on the fracture and mechanical properties of ceramics.

In this paper, a discrete element model of SiC ceramics is established and calibrated. Then, randomly oriented elliptical pore defects are introduced into the model by deleting particles. The effect of pore defect content and pore aspect ratio on the failure mode and mechanical properties of specimen is investigated under uniaxial compression. Finally, the effective Young's modulus obtained from the DEM simulations is compared with the theoretical curves of the Mori-Tanaka scheme and the Self-Consistent scheme at different pore defect densities.

2 Methodology

2.1 Discrete element method

In order to the study of the rock mechanics, the discrete element method was proposed by Cundall [20] in the 1970s. In DEM, the interaction between the contacting particles is a dynamic process. And the motion of the particles is governed by Newton's second law in any time step. The motion is divided into the translation and rotation. The corresponding equations of motion are as follow:

$$\text{Translation: } F_i - \beta_g v_i = m\frac{\Delta v_i}{\Delta t} \quad (1)$$

$$\text{Rotation: } M_i - \beta_g w_i = I\frac{\Delta w_i}{\Delta t} \quad (2)$$

where i (= 1, 2, 3) denotes the three components in x-, y-, z- direction; F_i is the out-of-balance force component of the particle; v_i is the translational velocity; m is the mass of the particle; M_i is the out-of-balance moment due to the contacts; w_i is the rotational velocity; I is the rotational inertia of the particle; β_g is the global damping coefficient; Δt is the time step.

In DEM, particles can be discrete free bodies [22], or bonded together at contact to form an assembly with arbitrary shapes, which can simulate bulk materials. The latter is called the BPM (bonded particle model) [23]. In the model, the particles are connected by parallel bonds, which can transfer the forces and moment between contacting particles, as shown in Figure 2. And the corresponding contact force F_c and the moment M_c are as follows:

$$\begin{cases} F_c = F^l + F^d + \overrightarrow{F} \\ M_c = \overrightarrow{M} \end{cases} \quad (3)$$

where F^l is the linear force; F^d is the dashpot force; $\overrightarrow{F}$ is the parallel bond force; $\overrightarrow{M}$ is the parallel bond moment.

The interaction force between the contacting particles includes a linear force F^l and a damping force F^d. The linear force is resolved into normal and shear components:

$$\begin{cases} F_n^{\,l} = \min((F_n^{\,l})_o + k_n\Delta\delta_n, 0), \\ F_s^{l} = \begin{cases} (F_s^{\,l})_o - k_s\Delta\delta_s, & no-slip \\ -\mu F_n^{l}, & slip \end{cases} \end{cases} \quad (4)$$

where $(F_n^l)_o$ and $(F_s^l)_o$ are the linear normal and shear force at the beginning of the time step, respectively; $\Delta\delta_n$ and $\Delta\delta_s$ are the relative normal and shear displacement increment at the contact during a time step, respectively; μ is the friction coefficient; k_n and k_s are the normal and shear stiffness values of particles, which can be calculated by knowing the particle effective modulus E^* and the particle normal-to-shear stiffness ratio κ^*.

The parallel bond force is resolved into a normal and shear components. And the parallel bond moment is resolved into a twisting and bending moment:

$$\begin{cases} \vec{F} = -\vec{F}_n n_c + \vec{F}_s & (\vec{F}_n > 0\, is\ tension) \\ \vec{M} = \vec{M}_t n_c + \vec{M}_b & (2D\text{model}: \vec{M}_t = 0) \end{cases} \quad (5)$$

When a parallel bond is created, the parallel bond force and moment are zeroed. Each subsequent relative displacement and rotation increment at the contact results in an increment in the elastic force and moment, which is added to the current values. In 2D model, the updated force and moment occurring over a time step of Δt are calculated as follows:

$$\text{parallel bond force: } \begin{cases} \vec{F}_n = \vec{F}_n + \vec{k}_n A\Delta\delta_n \\ \vec{F}_s = \vec{F}_s - \vec{k}_s A\Delta\delta_s \end{cases} \quad (6)$$

$$\text{parallel bond moment: } \vec{M}_b = \vec{M}_b - \vec{k}_n\Delta\theta_b\vec{I} \quad (7)$$

where $\vec{k}_n$ and $\vec{k}_s$ are the bond normal and shear stiffness, which can calculated by $\bar{E}^*$ and $\bar{\kappa}^*$; $\Delta\delta_n$ and $\Delta\delta_s$ are the relative normal and shear displacement increment respectively; A is the bond cross sectional area; $\vec{I}$ is the moment of inertia of the parallel bond cross-section; $\Delta\theta_t$ is the relative twist-rotation increment.

The maximum normal and shear stresses at the parallel bond periphery are calculated (via beam theory) as follows:

$$\begin{cases} \vec{\sigma} = \dfrac{-\vec{F}_n}{A} + \vec{\beta}\dfrac{\left|\vec{M}_b\right|\vec{R}}{\vec{I}} \\ \vec{\tau} = \dfrac{\left\|\vec{F}_s\right\|}{A} \end{cases} \quad (8)$$

If the maximum tensile stress exceeds the normal strength ($\vec{\sigma} \geq \sigma_{bond}$) or the maximum shear stress exceeds the shear strength ($\vec{\tau} \geq \tau_{bond}, \tau_{bond} = \vec{c} - \sigma\tan\vec{\phi}$), the parallel bond breaks. The relevant force, moment, and stiffness are then removed. When the parallel bonds break continually along a certain direction, microcracks formed between two particles will propagate along that direction accordingly [19].

At present, the BPM, which can present visually the initiation and propagation of microcracks in block materials, has been implemented in the researches of fracture, failure and machining process of hard and brittle materials such as geomaterials [25], concrete [26] and ceramics [27-28].

2.2 Modeling and calibration

In this paper, a BPM（bonded-particle model）with non-uniform-sized and densely packed particles was generated by PFC2D 5.0 software. Then, in order to make the established DEM model reflect the main mechanical properties of the actual SiC ceramics, it was necessary to specify the relevant properties of the particles and contact in the model. However, microscopic parameters at particle level (such as particle stiffness, parallel bond strength) could not be obtained directly through experimental measurements and there is no robust theory to directly relate the macro-scale material properties to their micro-scale counterparts. Therefore, numerical simulation tests in DEM are an appropriate approach to establish and calibrate the correlation between the mechanical properties of the material and the microscopic parameters of the particles and parallel bonds.

In the numerical tests, a uniaxial compression test (dimension of the model is 2 mm × 4 mm), a three-point bending test (dimension of the model is 3.6 mm × 0.75 mm, span is 3 mm) and a single edge notched beam test (dimension of the model is 3.6 mm × 0.75 mm, span is 3 mm, and incision height is 0.375 mm) were carried out, as shown in Fig. 3. Trial and error method was used to adjust the parameters in the model. When the results of DEM simulation test were close to the mechanical properties of the actual SiC ceramics, as shown in Table 1, it was considered that the microscopic parameters setting in the DEM model were reasonable. The microscopic parameters in discrete element model of SiC ceramic are listed in Table 2.

Table 1 Main mechanical properties of SiC ceramics from experiments and in DEM simulations

Mechanical properties	Experimental results[28]	DEM simulation
Elastic modulus (GPa)	420	419
Poisson's ratio	0.14	0.14
Compressive strength (MPa)	2000	1974
Bending strength (MPa)	500-800	639
Fracture toughness (MPa/m$^{1/2}$)	3.5	3.7

Table 2 The microscopic parameters in DEM model of SiC ceramic

Variable name(unit)	Symbol	Value
Minimum radius of particles(m) [23,27]	r_{min}	4.5e-6

Maximum-to-minimum radius ratio of particles	n	1.5
Density of particles(kg/m^3)	ρ	2600
Effective modulus of particles (Pa)	E^*	211e9
Normal-to-shear stiffness ratio of particles	κ^*	1.21
Bond effective modulus(Pa)	$\overline{E}^*$	211e9
Bond normal-to-shear stiffness ratio	$\overline{\kappa}^*$	1.21
Bond tensile strength(Pa)	$\overline{\sigma}_c$	7.8e8
Bond shear strength(Pa)	$\overline{\tau}_c$	50e8
Friction coefficient	μ	0.7
Bond gap	g	2e-7
Initial porosity of model [28-29]	p_0	0.16

3 DEM model of SiC ceramics containing random pore defects

3.1 Pore defect content

There are many microscale pore defects with various shapes in ceramic materials. In this paper, elliptical pores were considered in view of its common and representativeness. In the two-dimensional case, the pore defect content p is defined as follows:

$$p = \frac{1}{A}\pi\sum(ab)^{(k)} \tag{9}$$

where a and b denote the semi-major axis and the semi-minor axis of the elliptical pore, respectively; A is the specimen area, and k is the serial number of pores in the specimen.

For the case of the same size, the aspect ratio of elliptical pore may be different (the ratio of the semi-minor axis to the semi-major axis, defined as $Ar=b/a$). In view of this, the different aspect ratios (Ar=0.2, 0.5 and 1) were selected in this paper. And the size of each pore was the same in the generation process of pore. The corresponding calculation formulas of pore defect content p are presented in Table 3, where N is the number of pores.

When the pore defect content are identical, ie: $p_1 = p_2 = p_3$, the relationships between the values of semi-minor axis under different aspect ratios are as follows:

$$\frac{\sqrt{10}}{5}b_1 = b_2 = \sqrt{2}b_3 \tag{10}$$

Table 3 The corresponding calculation formulas of pore defect content under the different aspect ratios

Aspect ratio	Ar=0.2	Ar=0.5	Ar=1
Pore defect content	$p_1 = \frac{5N}{A}\pi b_1^{\,2}$	$p_2 = \frac{2N}{A}\pi b_2^{\,2}$	$p_3 = \frac{N}{A}\pi b_3^{\,2}$

*3.2 Random pore defect*s

By removing particles, elliptical pore defects were introduced into the established DEM model. The size, aspect ratio and orientation of pores are represented by elliptical equation and rotational transformation equation:.

$$\text{Elliptical equation:}\quad (\frac{x-x_0}{a})^2+(\frac{y-y_0}{b})^2=1 \quad (11)$$

$$\text{Rotational transformation equation:}\quad \begin{cases} x'=\cos\theta x+\sin\theta y \\ y'=-\sin\theta x+\cos\theta y \end{cases} \quad (12)$$

where a and b are the semi-major axis and the semi-minor axis of the elliptical pore defect respectively; x_0, y_0 are the center coordinates of the defect; x, y are the coordinates of the initial equation; x', y' are the coordinates of the equation after rotation; θ is the inclination angle between the semi-major axis of defect and the positive direction of the x-axis. Fig. 4 shows an example of the models containing elliptical pore defect with Ar = 0.5. The centre coordinates (x_0, y_0) of the pores were randomly generated in the model. And the inclination angles θ were 180° multiplied by a random number ranging from [-1, 1].

Taking Ar=0.5 as an example, the numbers of pore N were set as 10, 20, 30, 40, 50 (interval of 10) and the semi-minor axis b_2 were 20μm, 30μm, 40μm, 50μm; then, the corresponding relationships between the pore number N, the semi-minor axis b_2 and the pore defect content p_2 were established, as shown in Table 4. In addition, the cases where the aspect ratios Ar=0.2 and Ar=1 can also be obtained by the formula (10) and Table 3, which are not listed.

Table 4 The crelationship between pore number N, the semi-minor axis b_2 and pore defect content p_2

Pore Number N	***Semi-minor axis b_2***			
	20μm	**30μm**	**40μm**	**50μm**
10	0.0031	0.0071	0.0126	0.0196
20	0.0063	0.0141	0.0251	0.0393
30	0.0094	0.0212	0.0377	0.0589
40	0.0126	0.0283	0.0503	0.0785
50	0.0157	0.0353	0.0628	0.0982

4 Results and discussion

4.1 Effect of pore defect content on failure mode

In the uniaxial compression test, the compression loading obtained from two moving walls at the top and bottom of model was applied to the DEM model of the SiC ceramics with the random micropore defects. It was the criterion for loading stop and specimen failure that the current stress was lower than 80% of the peak stress in specimen. As illustrated in Fig. 5, the images of specimen failure are presented, in which the green lines represent the microcracks formed by the breakage of parallel bonds and the white parts are the elliptical pore defects. It can be observed that the increasing pore defect content results in obvious change on the type of macro-cracks in the failure specimen, presenting as different failure modes.

As shown in Figs. 5(a)-(h), when the pore defect content was relative low, which meant the small area and low number of pore defects, the internal microcracks explosively generated along the 60°-70° direction to form the shear macrocracks with rough fracture surface in the failure specimen. The failure mode of the specimen was brittle failure, similar to that of intact specimen under compression. It indicated that there was almost no interaction between the micropore defects because of relative low pore defect content.

As the pore defect content gradually increased (the area and the number of the internal pore defects increased accordingly), as shown in Figs. 5(i)-(o), there was an interaction between the adjacent pore defects under pressure. At the same time, except for the shear macroscopic crack formed by the large-scale explosion of microcracks, a new type of macroscopic crack was generated in failure specimen, which was evolved from the wing crack that initiated around the pore defect tips and propagated in the direction of the maximum principal stress (the axial loading direction in the text), as illustrated in Fig. 6. The failure mode of the specimen was the tensile-shear mixing.

Then, as the pore defect content increased continuously, as shown in Figs. 5(p)-(t), the interaction between the pore defects became stronger and stronger, which could affect the stress concentration in the specimen. The strong interaction made the wing cracks around the pore defects tips propagate easily, and then resulted in eventually a large amount of tensile coalescence between the adjacent pore defects. The tensile macroscopic cracks in coalescence, evolved from the wing cracks, were mostly slender and their fracture surfaces were smooth. Meanwhile, the failure mode of the specimen was mainly the axial tensile splitting. The crack propagation and damage behaviour in specimen with random pore defects were similar to those in specimen with random microcrack defects that we observed before [19]. It can be concluded that for the type of defect (random microcrack or micro pore), the failure mode of the specimen with defects under pressure will change correspondingly with the increase of the defect content.

4.2 Effect of aspect ratio on failure mode

In addition to the pore defect content, the influence of the pore shape on the failure mode cannot be ignored. Fig. 7 presents the images of the failure specimen with three aspect ratios of pores (pore number N=30 and pore defect content p=0.0212 were chosen as a representative case). More DEM tests were performed with five random pore distributions so that the random effect of the established model can be eliminated as much as possible. It can be observed that the distribution of the pore defect exerts an effect on the propagation path of the macrocrack in the failure specimen. Meanwhile, with the same pore defect content, the smaller the aspect ratio of the pore defects is, the more easily for the macro failure mode of the specimen changes from the brittle fracture (Fig. 7(a)) to the axial splitting (Fig. 7(c)). The reason is that the pore with a smaller aspect ratio has small the curvature radius at the pore tips, which leads to strong stress concentration effect and interaction between the pore defects. As a result, the wing cracks around the pore propagate easily after the initiation to form the macroscopic tensile cracks.

In summary, Table 5 shows the failure mode in the specimen with the different pore defect content and aspect ratio under uniaxial compression. With the increase of pore defect content p, the interaction between pore defects becomes stronger and stronger. The type of macroscopic crack in the failure specimen transfers from the original 60°-70° shear band to the tensile macrocrack, which direction is along the maximum principal stress (loading direction). The failure mode of the specimen changes from brittle fracture to tensile-shear mixing and finally to axial splitting. In addition, the change of the failure mode is related to the aspect ratio of the pore defects: the smaller the aspect ratio is, the easier the change is.

Table 5 Failure mode of specimen with random pore defects under uniaxial compression

Failure mode	Brittle fracture	Tensile-shear mix	Axial splitting
Pore defect content	Ar=0.5, $0<p<0.0157$	Ar=0.5, $0.0157<p<0.0393$	Ar=0.5, $0.0393<p<0.0982$
Example	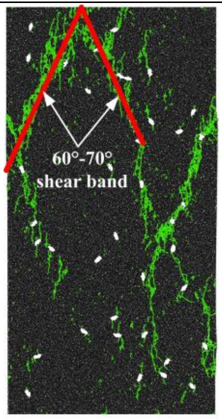 (20,40,0.0126)	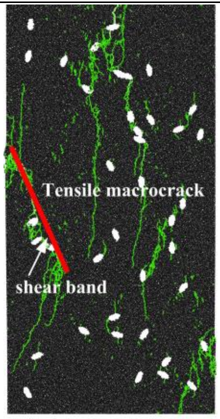 (30,40,0.0283)	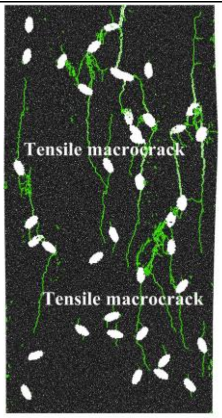 (40,40,0.0503)

Aspect ratio	Ar=1, p=0.0212	Ar=0.5, p=0.0212	Ar=0.2, p=0.0212
Example	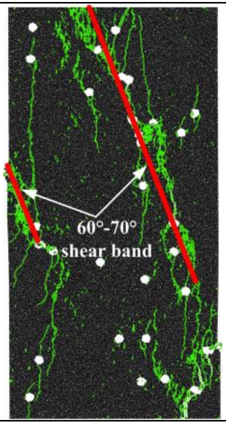	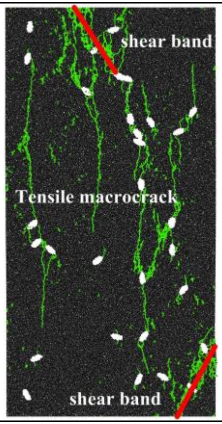	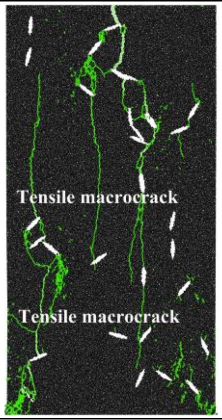

It is not difficult to see from the above results that the failure mode of the specimen is greatly affected by the defect content and the aspect ratio. Combining Table 3 and Table 4, by shorting the interval of pores number and adding the aspect ratios (Ar=1/3 and 1/4), more DEM simulations have been carried out. Fig. 8 roughly gives simplified diagram of the failure mode in the specimen with different pore defect content and the aspect ratios. In the figure, the abscissa is the reciprocal of the aspect ratio; the ordinate is the pore defect content. The data points are the critical values of the corresponding pore defect content at different aspect ratios when the failure mode is changed (the numerical results with five random pore distributions have presented). It can be seen that with the increase of pore defect content, the macro failure modes of the specimen are divided into three regions: A, B and C in the figure, which correspond to three failure modes respectively: brittle fracture, tensile-shear mixing and axial splitting.

When the pore defect content is low or high enough, the failure modes are brittle fracture or axial splitting accordingly and they are not affected by the aspect ratio of the pore. When the pore defect content is moderate, the flatter the pore defect is (the larger the $1/Ar$ is), the more easily for the failure mode changes from brittle fracture to tensile-shear mixing, or from tensile-shear mixing to axial splitting. In the meantime, it is worth noting that when the pore defect content is in a certain interval, as shown in the gray rectangular area (region D in Fig. 8), with the decrease of the aspect ratio Ar of the pore defects (the increase of the $1/Ar$), the failure mode of the specimen could transfer from brittle fracture to tensile-shear mixing and finally to axial splitting. The interval has been confirmed in Fig. 7 (the interval should be around p = 0.0212).

4.3 Analysis of mechanical properties

The pore defects with random orientation and position would affect the stress distribution in the specimen under pressure and the macroscopic mechanical properties of the specimen. Fig. 9 shows the curves of stress and crack initiation number with strain for aspect ratios: $Ar=0.2$, $Ar=0.5$ and $Ar=1$ at different pore defect content during loading. The crack initiation number is represented by the number of broken parallel bonds. It can be found from the figure that as the pore defect content increases, the slope of the stress-strain curve decreases continuously, which indicated the elastic modulus of the material decreased. Meanwhile, the value of peak stress and strain is also reduced correspondingly after the specimen failure and the bearing capacity of the specimen is greatly weakened. The crack initiation number has gradually increased from three stages during the loading: slow growth, rapid growth, exponential explosion growth. The larger pore defect content is prone to make the initiation and propagation of microcracks, which results in the failure specimen during the rapid growth stage. By comparison with previous studies, it can be found that the stress-strain curve and the crack initiation strain curve of the specimen with random pore defects are very similar to that of the specimen with microcrack defects [19]. In this process, the smaller the aspect ratio is, the more easily for the stress-strain curve change.

A sketch is generalized from the above numerical results to further analyze the stress-strain curves of the brittle materials with random defects under uniaxial compression, as shown in Fig. 10. The curves $OA_1B_1C_1$ and $OA_2B_2C_2$ represent the case of the specimen with low and high defect content respectively. During the initial loading, the stress-strain curves present the rising straight lines (section OA_1 and OA_2). The reason is that there is the linear elastic stage that is caused by the elastic deformation of the microdefects for the material. Besides, the strain in section OA_1 and OA_2: $O\varepsilon_{\mathrm{A1}}>O\varepsilon_{\mathrm{A2}}$.

Then, the curve reached the point of crack initiation. The reason why the slope of the corresponding curve showed a slight decrease and fluctuation (curve A_1B_1 and A_2B_2) was that before arriving at peak stress, the micro-damage in specimen appeared and some of microcracks were initiated and propagated stably. This process is known as a nonlinear hardening stage, represented by the strain: $\varepsilon_{\mathrm{A1}}\varepsilon_{\mathrm{B1}}>\varepsilon_{\mathrm{A2}}\varepsilon_{\mathrm{B2}}$, which shows that the load bearing capacity of specimens with low defect content is stronger at this stage, compared with that of high defect content.

Finally, the specimen reached the peak stress σ_{m}. The current stress of the specimen with low defect content decreases rapidly and the increasing microcracks exponentially make the specimen break down in an instant. This process is characterized by the rapid stress drop. However, the downtrend of current stress of the specimen with high defect content is slower and the strain is featured by certain “softening” (the downtrend of stress: section $B_1C_1>$ section B_2C_2 and strain: $\varepsilon_{\mathrm{B1}}\varepsilon_{\mathrm{C1}}<\varepsilon_{\mathrm{B2}}\varepsilon_{\mathrm{C2}}$).The reason is that the tensile coalescence between the internal defects was formed in the specimen with high defect content during loading and the fracture energy was absorbed, which played a certain role of “toughening”. It was generally recognized that after the specimen reached the peak stress, the steeper the line segment BC was, the larger the brittleness of material was. During the loading, the stress-strain curve of the specimen with low defect content presented the brittle fracture characteristics, while the stress-strain curve of the specimen with high defect content showed the plastic deformation characteristic because of axial tension splitting in the specimen.

The results of compressive strength and crack initiation stress were presented against different pore defect content and pore aspect ratio in Figs. 11 and 12 (the average results from five DEM simulations are used, and the error bar represents the standard deviation of the relevant results). It can be found that with the increase of the pore defect content, the compressive strength and crack initiation stress of the specimen are reduced nonlinearly. And a fluctuation of the error bars means that the randomness of the defect distribution has an influence on the strength of the specimen. It was larger for the decreasing trend of the compressive strength and crack initiation stress of the specimens with smaller pore defect content, which conformed that the brittle materials such as ceramics are sensitive to defects. Besides, it indicated that the low content of defects has an obvious effect on the strength of specimen. In addition, the specimen with the smaller aspect ratio of the pore defects featured as the lower the compressive strength and the crack initiation stress. This is because the pores with smaller the aspect ratios have the large stress concentration factor which depends on the curvature radius of pore. It results in the obvious interaction between the pores and the weaken strength and bearing capacity of specimen.

4.4 Comparison of effective Young's modulus

With respect to the discussion of the mechanical properties of solid materials with microdefects, the calculation of effective Young's modulus plays a significant role in the theoretical analysis of damage of brittle materials. Taking the elliptical pores as an example, the same pores area may have different aspect ratios. Therefore, Kachanov [32] added the eccentricity q on the basis of pore defect content p for the choice of parameters of the pores density, and the formula is as follows:

$$q=\frac{1}{A}\pi\sum(a-b)^2 \quad (13)$$

For the specimen with randomly oriented pores in the need of considering the defect interaction, the effective Young's modulus [32] in the Mori-Tanaka scheme and the Self-Consistent scheme are derived:

$$\text{Mori-Tanaka scheme:} \ \frac{E}{E_0}=\frac{1}{1+(3p+q)(1-p)^{-1}} \quad (14)$$

$$\text{Self-Consistent scheme:} \ \frac{E}{E_0}=1-(3p+q) \quad (15)$$

For the convenience, $3p+q$ is defined as the pore density [32]. Fig. 13 shows the comparison of effective Young's modulus of the DEM simulation with the predictions of the Mori-Tanaka scheme and the Self-Consistent scheme (SCS) at different pore densities. It can be seen that the results of the DEM simulation are coincide with the approximations of the Mori-Tanaka scheme and the self-consistent method at low pore densities. But when the pores density $3p+q$ is high, the DEM results are slightly lower than the theoretical result of Mori-Tanaka scheme. Two possible reasons are: (1) the established discrete element specimen has an initial porosity p_0, which derived from the gaps existed among the adjacent particles. And it may decrease the Young's modulus after the pore defects is introduced in specimen; (2) the strong interaction between the defects is considered in the DEM simulation at high defect densities, which resulted in the remarkable reduction of the effective modulus, while the Mori-Tanaka scheme, which only considered weak interaction between defects, has higher precision at low defect densities.

5 Conclusions

In this paper, a discrete element model of SiC ceramics with random micropore defects was established. The effects of pore defect content and aspect ratio on the failure modes and mechanical properties of SiC ceramic specimens were studied. Main conclusions are drawn as follow:

(1) The pore defect content and aspect ratio have a significant influence on the failure mode of specimen with randomly oriented micropore. With the increase of pore defect content, except for the shear macroscopic crack generated along the 60°-70° direction, a new type of macroscopic crack was generated in failure specimen, which is evolved from the wing crack that initiated around the pore defect tips and propagated in the direction of the axial loading. And the failure mode of specimen was changed from traditional brittle fracture to tensile-shear mixing, then to axial splitting. The smaller the aspect ratio was, the more easily for the failure mode changed.

(2) The stress-strain characteristics of specimens with high defect content and low defect content are distinctly different. In linear elastic stage and nonlinear hardening stage, the stress-strain curve of specimen with low defect content has a higher slope and larger strain. And a rapid drop of stress which indicated the material brittleness will happen after specimen reaches peak stress. However, the downtrend of current stress of the specimen with high defect content is slower and the strain is featured by certain “softening” due to tensile coalescence between the internal defects

(3) The compressive strength and crack initiation stress of the specimen decreased nonlinearly as the increase of pore defect content. And it was larger for above decreasing trend in the specimens with smaller pore defect content. The specimen with the smaller aspect ratio of the pore defects characterized as the lower the compressive strength and the crack initiation stress.

(4) The results of the effective Young's modulus obtained from discrete element simulation are fully consistent with that of the Mori-Tanaka scheme and the Self-Consistent scheme at low pore densities. But when the pores densities are large, the results of the discrete element simulation are slightly lower than that of the Mori-Tanaka scheme.

Acknowledgement

This work was supported by the National Natural Science Foundation of China (Grant No. 51605409, 51605410, 11772135 and 51606040)

Reference

[1]. A. Z. Wang, P. Hu, B. Du, Effect of collinear flaws on flexural strength and fracture behavior of ZrB_2-SiC ceramic, Ceram. Int.43 (2017) 14488-14492.

[2]. D. Munz, T. Fett, Ceramics: mechanical properties, failure behaviour, materials selection. Springer Science & Business Media, Berlin, 2013.

[3]. R. W. Davidge, Mechanical behaviour of ceramics. Cambridge University Press, Cambridge, 1979.

[4]. B. Budiansky, R. J. O'Connell, Elastic moduli of a cracked solid, Int. J. Solids. Struct. 12(1976) 81-97.

[5]. Y. Huang, K. X.Hu, A. Chandra, A generalized self-consistent mechanics method for microcracked solids, J. Mech. Phys. Solids. 42(1994)1273-1291.

[6]. Z. Hashin, The differential method and its application to cracked materials, J. Mech. Phys. Solids. 36(1988)719-734.

[7]. T. Mori, K. Tanaka, Average stress in matrix and average elastic energy of materials with misfitting inclusions, Acta. Metall. 21(1973)571-574.

[8]. Y. Benveniste, On the Mori-Tanaka's method in cracked bodies, Mech. Res. Commu. 13(1984)193-201.

[9]. X. Yang, X. Liu, Z. Huang, Vickers indentation crack analysis of solid-phase-sintered silicon carbide ceramics, Ceram. Int. 39(2013)841-845.

[10]. X. Yang, The effects of surface crack and inner defects on the mechanical properties of pressureless sintered silicon carbide ceramics. University of Chinese Academy of Sciences, Beijing, 2013.(in Chinese)

[11]. C. Petit, S. Meille, E. Maire, Mechanical behaviour of a β-TCP ceramic with a random porosity: Study of the fracture path with X-ray tomography, J. Eur. Ceram. Soc. 36(2016)3225-3233.

[12]. C. Sklarczyk, The acoustic emission analysis of the crack processes in alumina, J. Eur. Ceram. Soc. 9(1992)427-435.

[13]. H. Li, L. N. Y. Wong, Influence of flaw inclination angle and loading condition on crack initiation and propagation, Int. J. Solids. Struct. 49(2012)2482-2499.

[14]. Z. Wu, L. N. Y. Wong, Frictional crack initiation and propagation analysis using the numerical manifold method, Comput. Geotech. 39(2012)38-53.

[15]. C. J. Pearce, A. Thavalingam, Z. Liao, Computational aspects of the discontinuous deformation analysis framework for modelling concrete fracture, Eng. Fract. Mech. 65(2000)283-298.

[16]. C. S. Chen, E. Pan, B. Amadei, Fracture mechanics analysis of cracked discs of anisotropic rock using the boundary element method, Int. J. Rock. Mech. Min. 35(1998)195-218.

[17]. C. A. Tang, S. Q. Kou, Crack propagation and coalescence in brittle materials under compression, Eng. Fract. Mech. 61(1998)311-324.

[18]. Wong. R. H. C, P. Lin, Numerical study of stress distribution and crack coalescence mechanisms of a solid containing multiple holes, Int. J. Rock. Mech. Min. 79(2015)41-54.

[19]. S. Q. Jiang, X. Li, Y. Q. Tan, Discrete element simulation of SiC ceramic with pre-existing random flaws under uniaxial compression, Ceram. Int. 43(2017)13717-13728.

[20]. P. A. Cundall, A computer model for simulating progressive large scale movements in blocky system, Proc. Int. symp. on Rock Fracture. 1(1971) 8-11.

[21]. P. A. Cundall, O. D. L. Strack, discrete numerical model for granular assemblies, geotechnique. 29(1979) 47-65.

[22]. S. Q. Jiang, Y. X. Ye, Y. Q. Tan, Discrete element simulation of particle motion in ball mills based on similarity, Powder. Technol. 335(2018) 91-102.

[23]. D. O. Potyondy, P. A. Cundall, A bonded-particle model for rock, Int. J. Rock. Mech. Min. 41(2004) 1329-1364.

[24]. N. Cho, C. D. Martin, D. C. Sego, A clumped particle model for rock, Int. J. Rock. Mech. Min. 44(2007)997-1010.

[25]. L. A. M. Camones, E. D. A. V. Jr, R. P. D. Figueiredo, Application of the discrete element method for modeling of rock crack propagation and coalescence in the step-path failure mechanism, Eng. Geol. 153(2013)80-94.

[26]. S. Hentz, F. V. Donzé, L. Daudeville, Discrete element modelling of concrete submitted to dynamic loading at high strain rates, Comput. Struct. 82(2004)2509-2524.

[27]. Y. Q. Tan, D. M. Yang, Y. Sheng, Study of polycrystalline Al_2O_3 machining cracks using discrete element method, Int. J. Mach. Tools. Manu. 48(2008)975-982.

[28]. Y. Q. Tan, D. M. Yang, Y. Sheng, Discrete element method (DEM) modeling of fracture and damage in the machining process of polycrystalline SiC, J. Eur. Ceram. Soc. 29(2009)1029-1037.

[29]. H. Huang, Discrete element modeling of Tool-Rock Interaction. University of Minnesota, Minnesota, 1999.

[30]. M. Sagong, A. Bobet, Coalescence of multiple flaws in a rock-model material in uniaxial compression, Int. J. Rock. Mech. Min. 39(2002)229-241.

[31]. A. Bobet, H. H. Einstein, Fracture coalescence in rock-type materials under uniaxial and biaxial compression, Int. J. Rock. Mech. Min. 35(1998)863-888.

[32]. M. Kachanov, I. Tsukrov, B. Shafiro, Effective moduli of solids with cavities of various shapes, Appl. Mech. Rev. 47(1994)50-57.

List of figure captions:

Fig. 1. SEM images of typical defects of ZrB_2-SiC ceramics in Ref. [1]
Fig. 2. Parallel-bonded (ball-ball) contacts in BPM [24]
Fig. 3. Calibration tests of micro parameters in DEM
Fig. 4. (a) Model with random pores (b) DEM model containing random pore defects
Fig. 5. Failure model of specimen (b_2, N, p) with different pore defect content p
Fig. 6. Initiation and propagation of crack around the pore defect under pressure (revised in Ref. [30])
Fig. 7. Images of failure specimen with five random distribution of pore defects, (a)Ar=1, (b)Ar=0.5, (c)Ar=0.2.
Fig. 8. Schematic diagram of failure mode of specimen with random pore defects
Fig. 9. Stress-strain curve and crack initiation number-strain curve under different pore defect content for three different aspect ratios, (a)Ar=0.2, (b)Ar=0.5, (c)Ar=1
Fig. 10. Stress-strain curves in the failure process of specimens with two types of defect contents (low defect content: $OA_1B_1C_1$, high defect content: $OA_2B_2C_2$)
Fig. 11. Compressive strength vs. pore defect content for three aspect ratios
Fig. 12. Crack initiation stress vs. pore defect content for three aspect ratios
Fig. 13. Comparison of DEM simulation with Mori-Tanaka scheme and Self-Consistent scheme for randomly oriented elliptical pores of different aspect ratios, (a)Ar=0.2, (b)Ar=0.5, (c)Ar=1

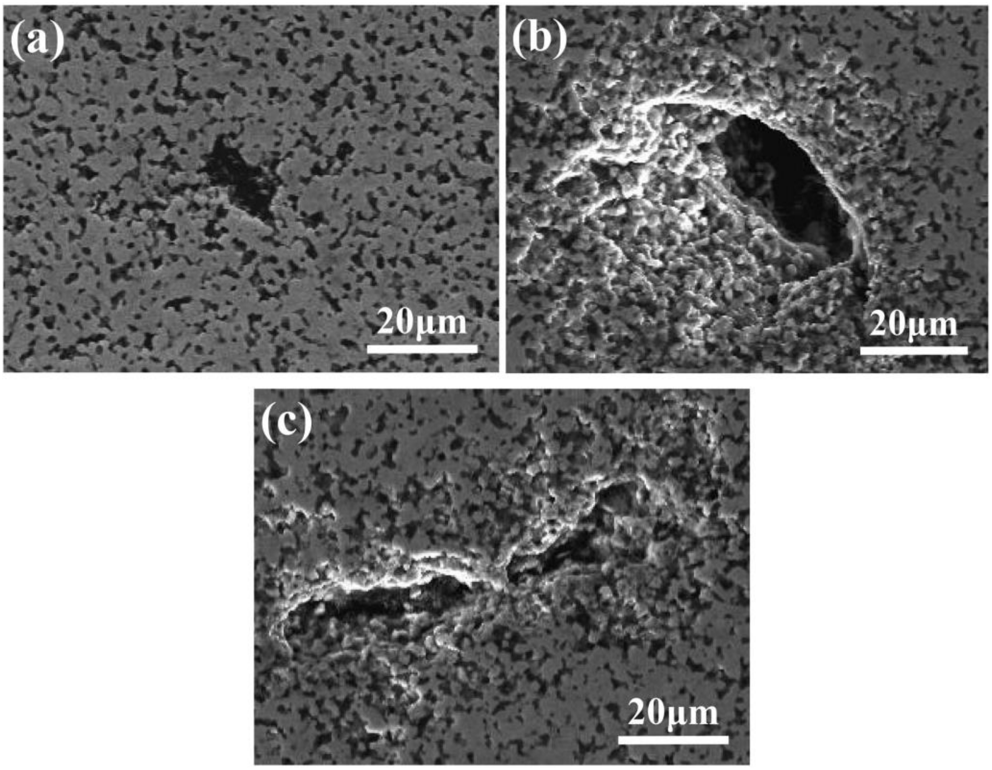

Fig. 1. SEM images of typical defects in SiC ceramics [1]

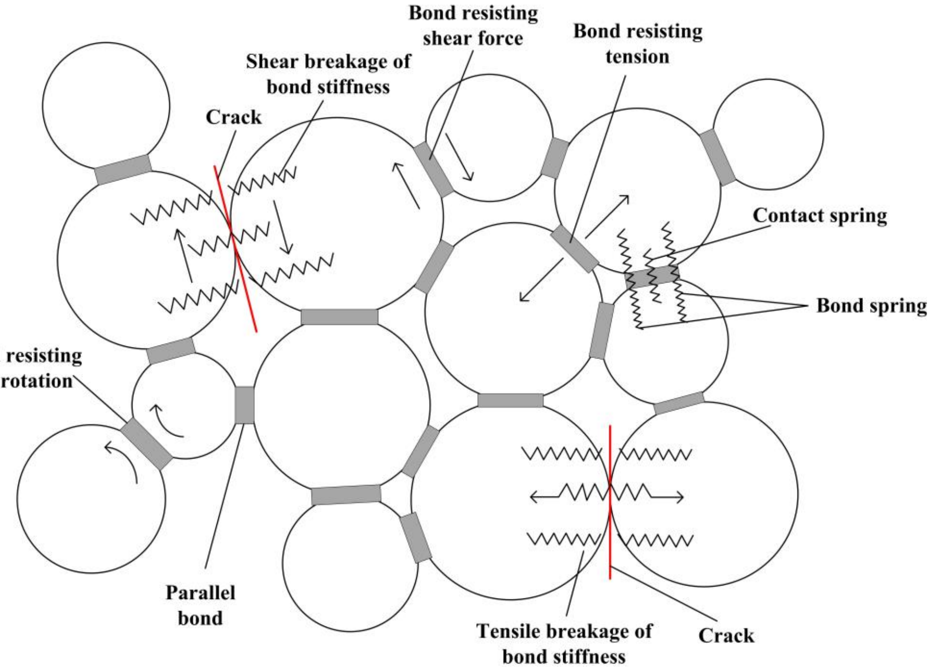

Fig. 2. Parallel-bonded (ball-ball) contacts in BPM [24]

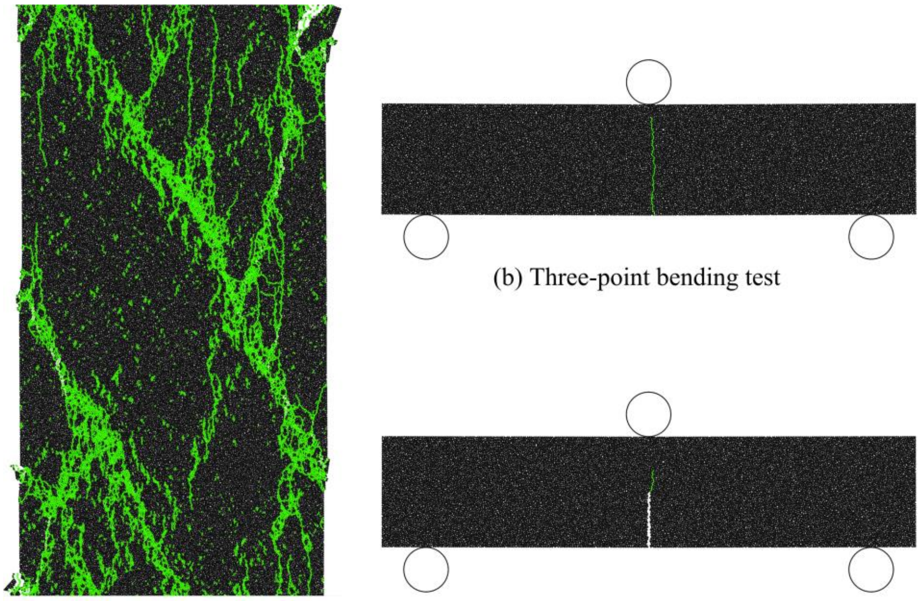

(a) Uniaxial compression test

(b) Three-point bending test

(c) Single edge notched beam test

Fig. 3. Calibration tests of micro parameters in DEM

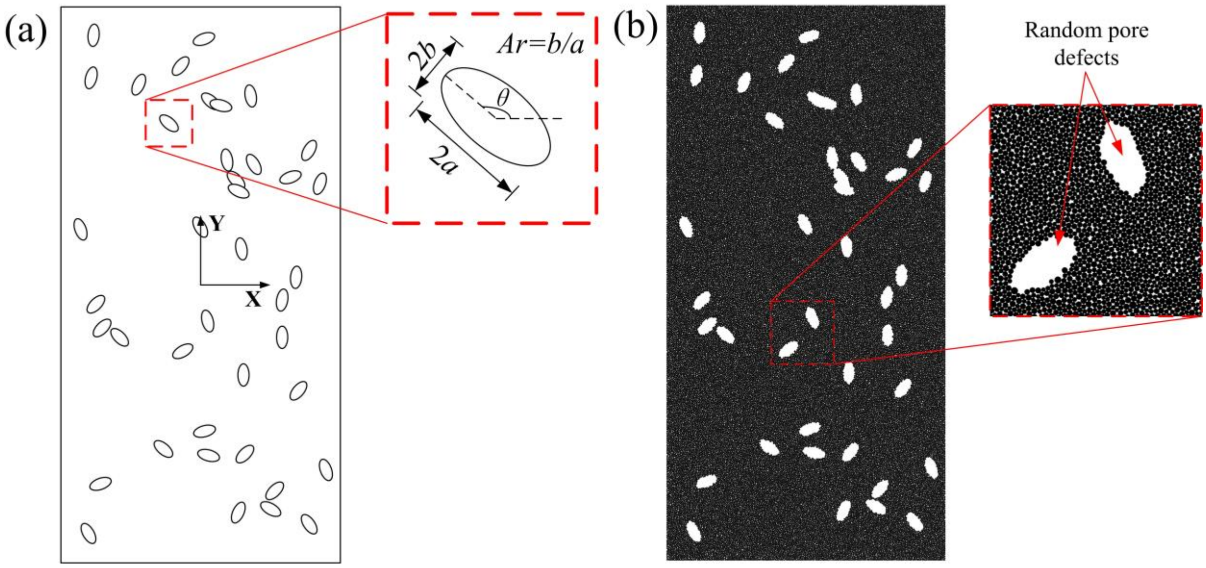

Fig. 4. (a) Model with random pores (b) DEM model containing random pore defects

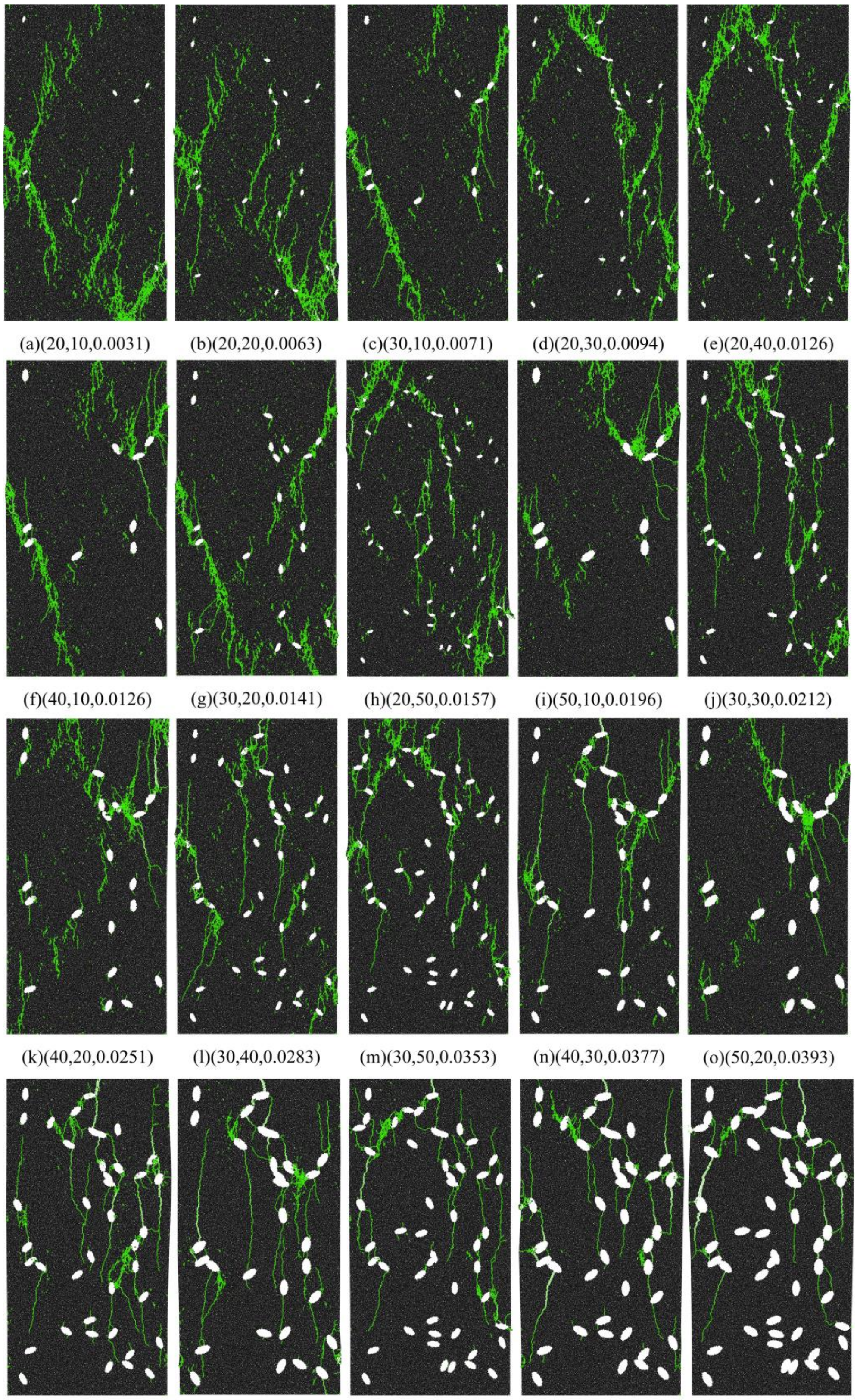

(a)(20,10,0.0031) (b)(20,20,0.0063) (c)(30,10,0.0071) (d)(20,30,0.0094) (e)(20,40,0.0126)

(f)(40,10,0.0126) (g)(30,20,0.0141) (h)(20,50,0.0157) (i)(50,10,0.0196) (j)(30,30,0.0212)

(k)(40,20,0.0251) (l)(30,40,0.0283) (m)(30,50,0.0353) (n)(40,30,0.0377) (o)(50,20,0.0393)

(p)(40,40,0.0503) (q)(50,30,0.0589) (r)(40,50,0.0628) (s)(50,40,0.0785) (t)(50,50,0.0982)

Fig. 5. Failure model of specimen (b_2, N, p) with different pore defect content p

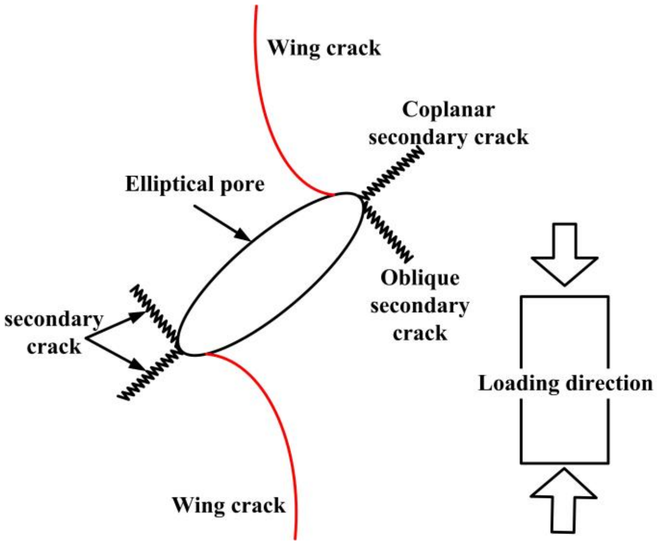

Fig. 6. Initiation and propagation of crack around the pore defect under pressure (revised in Ref. [30])

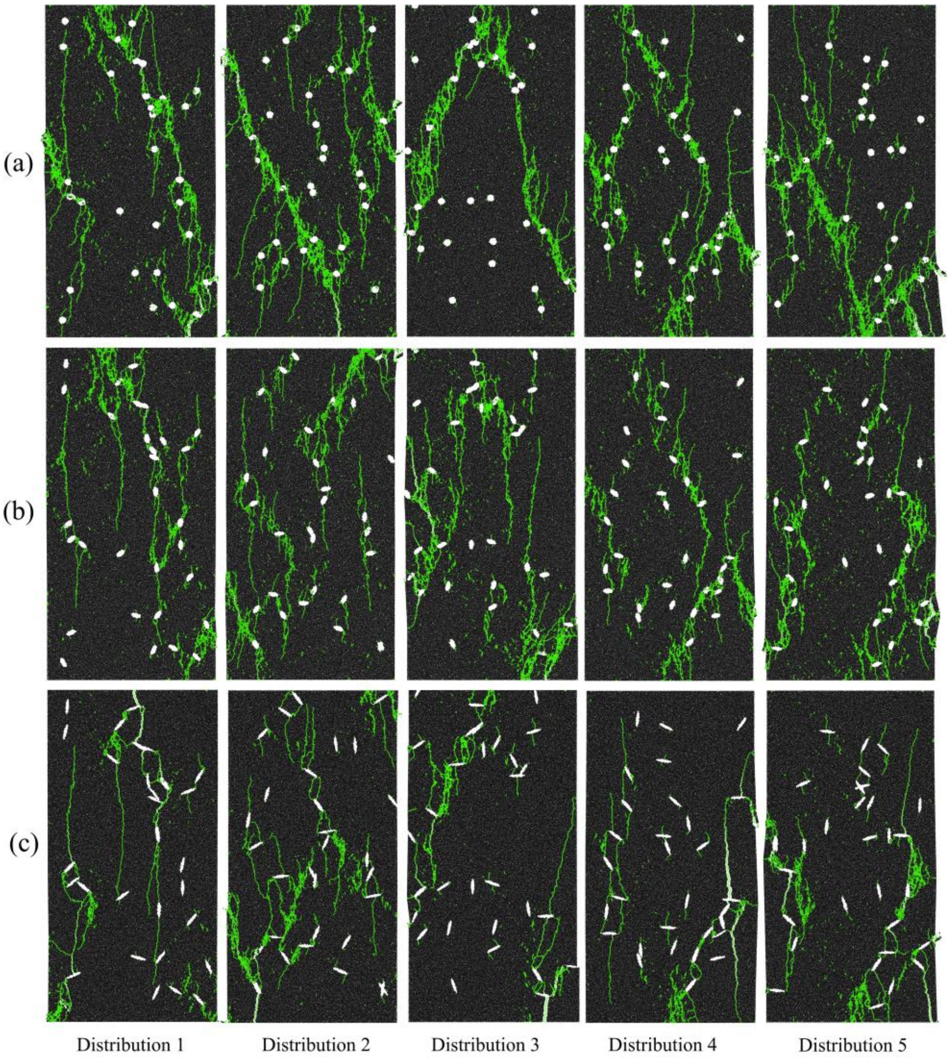

Fig. 7. Images of failure specimen with five random distribution of pore defects (a)*Ar*=1, (b)*Ar*=0.5, (c)*Ar*=0.2.

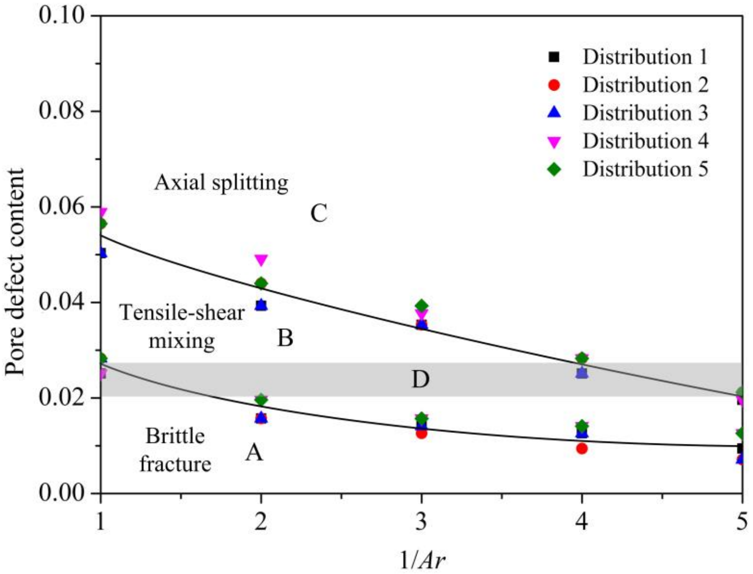

Fig. 8. Schematic diagram of failure mode of specimen with random pore defects

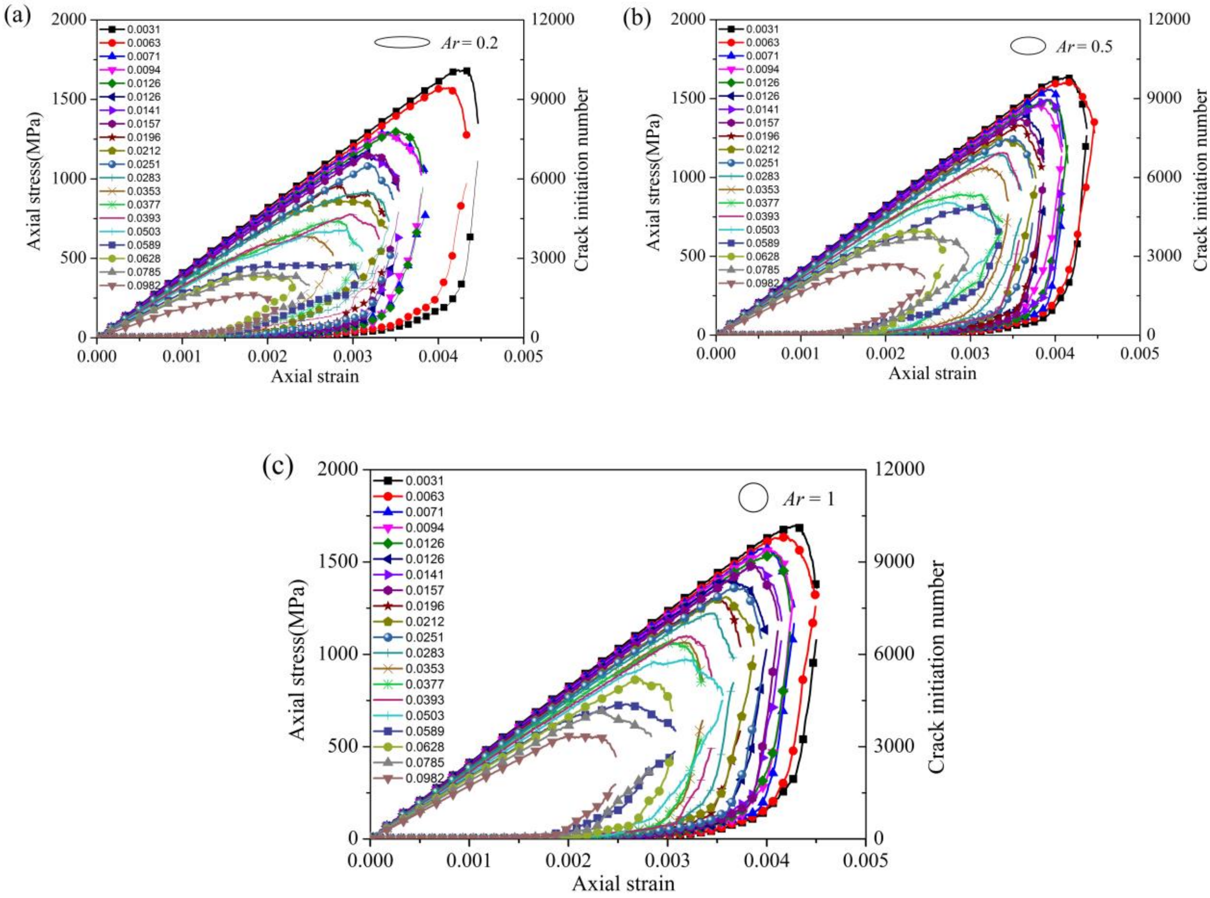

Fig. 9. Stress-strain curve and crack initiation number-strain curve under different pore defect content for three different aspect ratios, (a)*Ar*=0.2, (b)*Ar*=0.5, (c)*Ar*=1

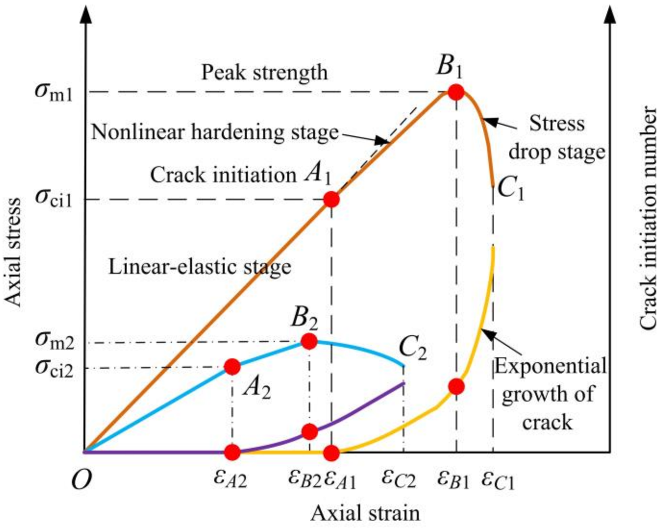

Fig. 10. Stress-strain curves in the failure process of specimens with two types of defect contents (low defect content: $OA_1B_1C_1$, high defect content: $OA_2B_2C_2$)

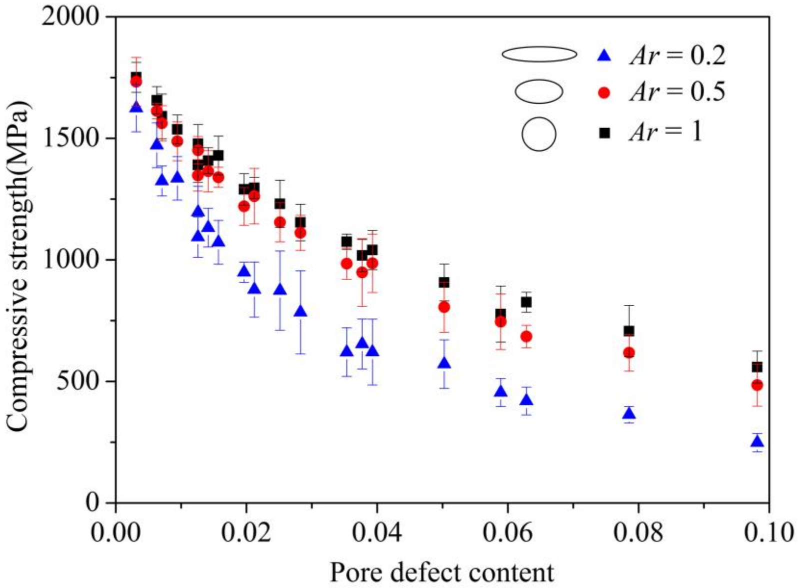

Fig. 11. Compressive strength vs. pore defect content for three aspect ratios

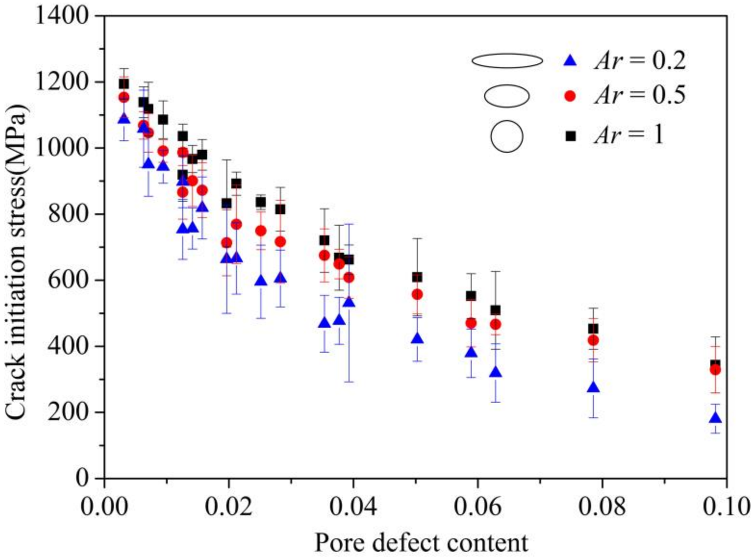

Fig. 12. Crack initiation stress vs. pore defect content for three aspect ratios

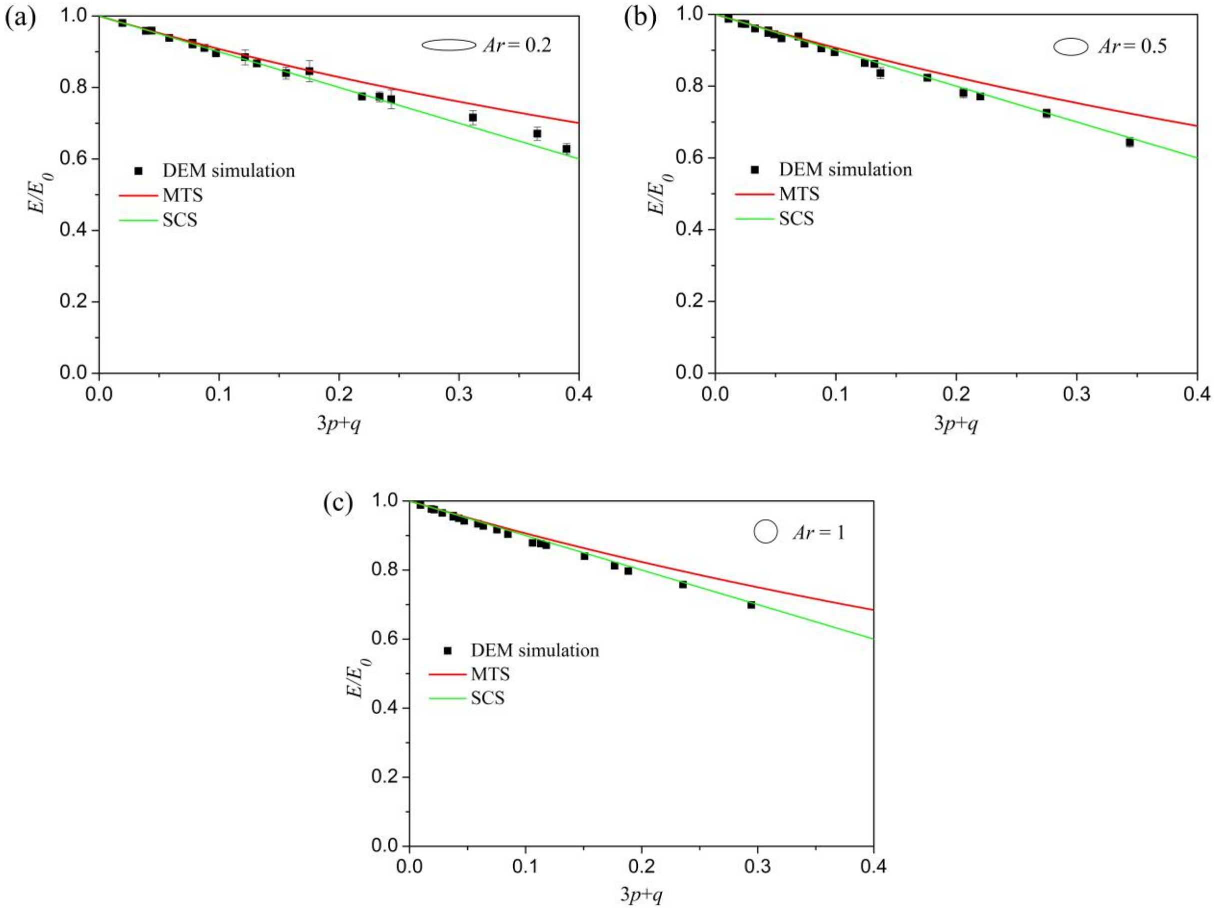

Fig. 13. Comparison of DEM simulation with Mori-Tanaka scheme and Self-Consistent scheme for randomly oriented elliptical pores of different aspect ratios, (a)Ar=0.2, (b)Ar=0.5, (c)Ar=1